Semitransparent Perovskite Solar Cell With Sputtered Front and Rear Electrodes for a Four-Terminal Tandem

The Duong, Niraj Lal, Dale Grant, Daniel Jacobs, Peiting Zheng, Shakir Rahman, Heping Shen, Matthew Stocks, Andrew Blakers, Klaus Weber, Thomas P. White, and Kylie R. Catchpole

Abstract—A tandem configuration of perovskite and silicon solar cells is a promising way to achieve high-efficiency solar energy conversion at low cost. Four-terminal tandems, in which each cell is connected independently, avoid the need for current matching between the top and bottom cells, giving greater design flexibility. In a four-terminal tandem, the perovskite top cell requires two transparent contacts. Through detailed analysis of electrical and optical power losses, we identify optimum contact parameters and outline directions for the development of future transparent contacts for tandem cells. A semitransparent perovskite cell is fabricated with steady-state efficiency exceeding 12% and broadband near infrared transmittance of >80% using optimized sputtered indium tin oxide front and rear contacts. Our semitransparent cell exhibits much less hysteresis than opaque reference cells. A four-terminal perovskite on silicon tandem efficiency of more than 20% is achieved, and we identify clear pathways to exceed the current single silicon cell record of 25.6%.

Index Terms—Perovskite, silicon, solar energy, tandem.

I. Introduction

PEROVSKITE solar cells have emerged as the new key material for the photovoltaic community with certified efficiency reaching 20.1% after six years of development [1]. With a tunable high band gap for the active material (1.55–2.3 eV), perovskite cells are an ideal candidate for the top cell in a tandem configuration with a silicon bottom cell [2]. Several recent studies have shown the potential for such tandem cells to exceed efficiencies of 30%, but this requires careful light management and minimization of optical losses [3]–[5].

There are two possible tandem configurations: two-terminal and four-terminal. While offering potentially lower costs and a requirement of only one transparent contact, the two-terminal tandem requires current matching between top and bottom cells and an efficient tunneling junction between the two subcells.

This has limited the efficiency of the two-terminal tandem to 18% to date [6], [7]. The four-terminal tandem does not require current matching, instead only requiring an optical coupling layer between the two subcells. Although introducing additional complexity, the four-terminal tandem allows individual cells to be optimized separately yielding greater flexibility in the cell design. The four-terminal tandem, however, requires transparent contacts at both front and rear, which are the biggest challenge to reaching high efficiency. Optical absorption in these contacts is a main source of photocurrent loss in both top and bottom cells. While it is possible to reduce these losses by making the contacts thinner, or reducing the level of doping, this reduces their conductivity and can thus lead to voltage loss in the perovskite top cell. Therefore, optimizing transparent contacts to balance optical and electrical losses is crucial.

A further challenge is the process incompatibility and low thermal budget of organic layers in current perovskite cells, which limits the material and deposition techniques for the rear transparent contact. As the first experimental demonstration of the perovskite-on-silicon tandem cell, Löper *et al.* reported a tandem efficiency of 13.4% with semitransparent perovskite cell using FTO as the front contact and sputtered ITO as the rear contact [8]. The semitransparent perovskite cell efficiency was 6.2% and the long-wavelength transparency was limited to 60%. The development of Ag nanowires as the rear transparent contact using a mechanical transfer process enabled an efficiency of 18.6% for perovskite on copper indium gallium selenide and 17.0% for perovskite on silicon cells [9]. The transmittance of the semitransparent perovskite in this case was improved significantly to as high as 77% peak at a wavelength of around 800 nm. However, the use of silver electrodes affects the stability of the device through the formation of silver iodide, which quickly degrades the cell performance [10]. The best tandem efficiency reported to date is 19.5%, using a semitransparent perovskite cell fabricated with aluminum doped zinc oxide (AZO) as the rear transparent contact [11]. The performance of the perovskite top cell was much improved by optimizing the sputtering condition for the rear transparent contact; however, the average transmittance of the device in the wavelength region 800–1000 nm was limited to 71%, mainly caused by absorption in the FTO front contact and the 400-nm-thick AZO rear contact. Other materials such as dielectric–metal–dielectric stacks, adhesive laminate material, and graphene have been applied as rear transparent contacts for semitransparent perovskite cells;

however, the performance of these cells is less than 12%, with subbandgap transparency ∼60% [12]–[16].

In this work, we perform a detailed power loss analysis of the tandem efficiency resulting from the nonideal properties of the transparent contacts at the front and rear sides of perovskite cells. By optimizing sputtered ITO for both front and rear contacts, we demonstrate semitransparent mesoporous $CH_3NH_3PbI_3$ perovskite cell exceeding 12% efficiency and surpassing 80% transmittance in the 800–1000 nm wavelength range. Optical modeling of the complete cell structure shows good agreement with experimental data, allowing quantification of the major sources of current loss, and a clear design strategy to further improve tandem efficiency.

II. Result and Discussion

A. Detailed Calculation of the Power Losses of a Tandem Cell With Transparent Contacts

In this section, we perform a detailed analysis of optical (transmission) and electrical (resistive) losses introduced by semitransparent top cell contacts in a four-terminal perovskite-on-silicon tandem. This analysis helps to identify the target range of interest for sheet resistance and transmittance of contact layers to achieve optimal tandem efficiency.

For the power loss analysis, we take as a reference a tandem consisting of a state-of-the-art 17.7% efficient $CH_3NH_3PbI_3$ perovskite cell and a 25.0% efficient silicon cell. These cells were chosen to meet our ultimate aim of achieving efficiencies above 25%; however, the conclusions drawn from the analysis are equally valid for lower efficiency cell combinations.

The reference perovskite cell characteristics are set as $J_{sc,p} = 22.1 \, mA/cm^2$, $V_{oc,p} = 1.00 \, V$, $FF_p = 0.8$. For the Si cell, we assume that the perovskite top cell acts as a long-pass filter, only transmitting subbandgap light with $\lambda > 800$ nm ($E_g = 1.55$ eV). Under this reduced spectrum, the reference Si cell characteristics are $J_{sc,Si} = 16 \, mA/cm^2$, $V_{oc,Si} = 0.68 \, V$, and $FF_{Si} = 0.828$ [3], [17], [18]. The reference power (P_0) for the four-terminal tandem with no additional optical or electrical losses is the sum of the two individual cell outputs

$$P_0 = J_{sc,Si} \times V_{oc,Si} \times FF_{Si} + J_{sc,p} \times V_{oc,p} \times FF_p$$

which gives a power of 26.7 mW/cm^2 or a tandem efficiency of 26.7%.

We next consider the impact of nonunity transmittance and nonzero sheet resistance in the front and rear contacts of the top cell. For each contact, we calculate a total tandem power loss ΔP that is the sum of electrical and optical losses, noting that to first order, electrical losses impact only on the cell voltage while optical losses impact on the cell current. From this, we define the power fraction relative to the reference power:

$$\frac{P}{P_0} = 1 - \frac{\Delta P}{P_0}.$$

The power fraction is a function of the contact transmittance (T), which we approximate as a constant value for all wavelengths, and an effective contact sheet resistance R'_{sh} accounts for the sheet resistance R_{sh} of the conducting semitransparent film (ITO or FTO), plus any additional metal gird lines used to improve the conductivity. A detailed definition of R'_{sh} is given in the supplementary material section.

The tandem cell power loss due to the front contact can be divided into three contributions:

$$\Delta P_{front} = P_{R,p} + P_{T,p} + P_{T,Si}$$

where $P_{R,p}$ and $P_{T,p}$ are the resistive and optical power losses in the top (perovskite) cell, respectively, and $P_{T,Si}$ is the optical power loss in the silicon due to nonunity transmission of subbandgap light through the top cell. Full expressions for each of these terms are provided in the supplementary information.

The rear contact loss has only two contributions since nonunity transmission through the rear contact does not impact the top cell:

$$\Delta P_{rear} = P_{R,p} + P_{T,Si}$$

where the expressions for $P_{R,p}$ and $P_{T,Si}$ are identical to those used for the front cell.

Fig. 1 shows contour plots of the power fraction as a function of T and R_{sh}, calculated separately for the front (a) and rear (b) contacts. Results were calculated for a tandem cell area of 1 cm^2, and we assume that current from the top cell is collected via parallel busbars separated by 1 cm. As can be seen from Fig. 1(a), when $R_{sh} < 10 \, \Omega/\square$, the power loss is dominated by transmission losses and the power fraction is almost independent of R_{sh} (indicated by the near-horizontal contour lines). With higher sheet resistance of 100 $\Omega/\square$, the maximum power fraction that can be achieved is about 80%, with perfect transmittance of the layer. To achieve 90% power fraction, the layer sheet resistance needs to be less than 70 $\Omega/\square$ in the case of perfect transmittance, and the sheet resistance needs to be lower with reduced transmittance. Thus, the range of interest for the front contact is less than 70 $\Omega/\square$ for the sheet resistance and >90% for the transmittance (or absorption less than 10% when reflectance is neglected). For the rear contact as presented in Fig. 1(b), to achieve 95% power fraction, the sheet resistance needs to be lower than 30 $\Omega/\square$ and the transmittance needs to be higher than 85%. The white spots in both figures indicate experimentally measured sheet resistance and transparency for thin sputtered ITO layers using different deposition conditions, as discussed in the following sections. The arrows and black spots in Fig. 1(b) indicate the increase in power fraction that can be achieved by depositing a grid of 35-μm-wide, 100-nm-thick gold fingers with a 1-mm pitch onto the rear ITO film to transport current to the busbars. These grid lines introduce a small additional optical loss, but significantly reduce the electrical losses, resulting in a net power gain from the tandem cell. The parameters of the grid correspond to those used in our fabricated semitransparent cells described below, although there is a great deal of freedom to vary these depending on fabrication constraints. The method of calculating the effective sheet resistance and effective transparency of the transparent contacts with metal grids is described in the supporting material. Although we have not considered it here due to fabrication challenges, the addition of gridlines in the front contact could further improve the cell performance.
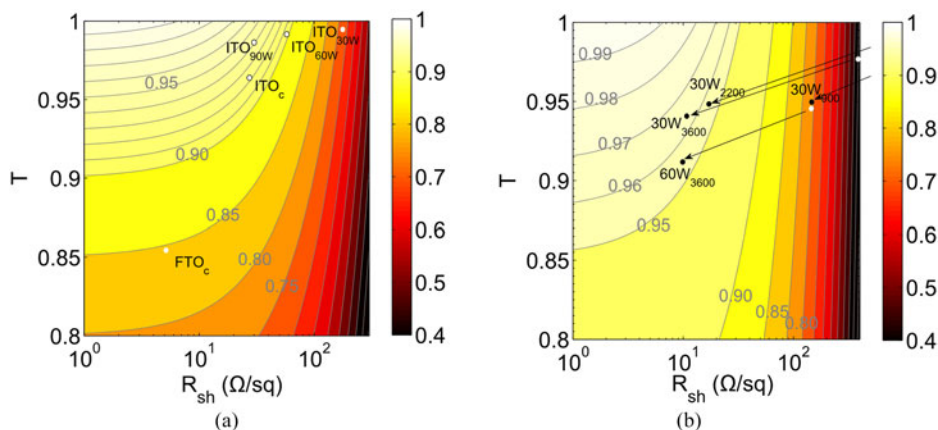
Fig. 1. Power loss analysis of tandem efficiency coming from the nonideal electrical and optical properties of the front transparent contact (a) and rear transparent contact (b). The points correspond to experimental data of commercial FTO (FTO$_C$), commercial ITO (ITO$_C$), and sputtered ITO substrates developed in this work. No metal grid was applied for the front contact; hence, the white points in (a) indicate the sheet resistance and transparency of bare TCO films. The white points of origin of the arrows in (b) indicate the sheet resistance and transparency of the bare TCO film, while the black points indicate the effective sheet resistance and transparency after the implementation of metal grids with parameters given in the main text.

In the following sections, we describe the experimental optimization of front and rear ITO electrodes in a semitransparent perovskite cell with reference to the above power loss analysis, as well as other process-related constraints.

B. Front Contact Optimization

In this section, we describe the development of a front transparent contact for the perovskite top cell using sputtered ITO on glass substrate. A metal grid was not applied for the front transparent contact due to the incompatibility with the perovskite cell fabrication process. The sheet resistance, absorption, and power fraction of the substrate when used as the front contact on perovskite cell was then compared with the widely used commercial FTO and commercial ITO substrates. While commercial FTO substrates normally have low sheet resistance (7 $\Omega/\square$ for TEC 7) and can withstand high-temperature processes, the excessive absorption of up to 30% in the long-wavelength region makes them unsuitable for the superstrate contact in perovskite cells, especially in a tandem structure. Commercial ITO with low sheet resistance of 8–12 $\Omega/\square$ also has absorption of up to 15% in the long-wavelength part of the spectrum [see Fig. 2(a)]. We have found that with a high-temperature annealing step of up to 500 °C in air required for the fabrication of mesoporous perovskite cells, the sheet resistance of the commercial ITO substrate increases to 25–30 $\Omega/\square$, and the absorption is reduced but is still more than 7%, as in Fig. 2(a).

In this work, we have optimized an RF sputtering process to deposit ITO films with absorption below 4% and sheet resistance comparable to commercial ITO (26.7 $\Omega/\square$ after annealing). The absorption and sheet resistance of the films are further reduced after high-temperature annealing at 500 °C in air. The RF power and deposition duration is varied while keeping chamber pressure fixed to achieve different film transmittance and sheet resistances. Fig. 2(a) shows the measured absorption of various TCO films on glass substrates and their sheet resistance values before and after high-temperature annealing in air. The lower absorption and higher transmittance of the sputtered ITO after

annealing are explained by the improvement in the crystal structure and the oxidation of compounds with lower valence states which appear brownish or black [19]. Fig. S3, in the supplementary material, shows XRD results of the ITO film before and after annealing in air. The film is amorphous after deposition and becomes crystalline after annealing. The reason for the reduction of sheet resistance is still unknown and is contradictory to other reports [20], [21]. Nonetheless, the impact of annealing conditions on the electrical and optical properties of ITO film is known to be very sensitive to deposition conditions and technique [20]–[24]. The roughness of the sputtered ITO as measured by atomic-force microscopy (AFM) is comparable with the commercial ITO and is much smaller than the roughness of FTO substrate. The roughness average decreases from the root-mean-squared value Rq of 5.4–1.6 nm after high-temperature annealing. The AFM images of all the substrates are presented in Fig. S3, available in the supplementary material.

The optical properties of the glass substrate are also important since the absorption of glass in the near infrared varies from less than 1% for quartz to 3–4% in normal microscope slide glass. Fig. S4, in the supplementary material, shows the comparison of transmittance between sputtered ITO on different glass types.

The projected power losses in a perovskite-on-silicon tandem cell using the commercial FTO, commercial ITO and various sputtered ITO substrates as the front transparent contact are indicated by the white points in Fig. 1(a). To account for the non-flat transmittance spectrum of the layer, solar weighted transmittance is calculated with the assumption of no reflectance. From the analysis, FTO substrates offer a tandem efficiency power fraction of less than 85% compared with the ideal case, mainly due to the high absorption of the FTO layer. Sputtered ITO at 30 W offers less than 70% power fraction, mainly due to the resistive power loss from the high sheet resistance of the layer. Transparent contacts with sputtered ITO at RF power of 60 W, 90 W, and commercial ITO lie in the range of interest. Sputtered ITO at RF power of 90 W gives the best power fraction of 94% as the result of high transparency
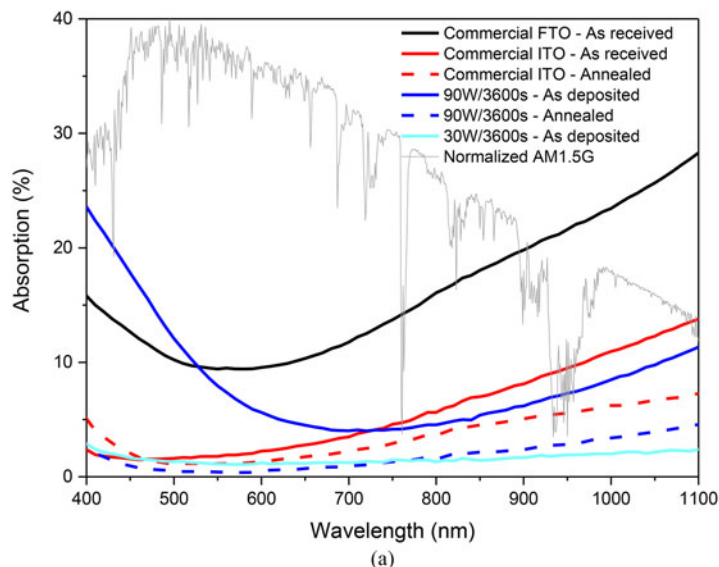
Substrate	Power (W)	Time (s)	Film Thickness (nm)	Sheet Resistance (Ω/□)		Solar-weighted Absorption (%)	
				As Deposited	Annealed	As Deposited	Annealed
Commercial FTO			650	6.2	4.9	15.3	14.8
Commercial ITO			110	10.8	26.7	5.2	4.2
Sputtered ITO	90	3600	95	58	29.8	10.1	2.2
Sputtered ITO	60	3600	82	151	57.7	5.4	1.7
Sputtered ITO	30	3600	45	401	174.8	2.6	1.3
Sputtered ITO	30	2200	35	900		2.1	
Sputtered ITO	30	900	15	~10000		1.8	

(b)

Fig. 2.   (a) Measured absorption of different transparent contacts for the front and rear electrodes. The AM1.5G solar spectrum is shown for reference. Only selected sputtered ITO substrates are presented for clarity. (b) Film thickness, sheet resistance, and solar weighted absorption of different transparent contacts before and after annealing.

and reasonably low sheet resistance. In real cases, reflectance (which has been neglected in this analysis since it will depend greatly on the structure, layer thickness, and surface roughness of the device) would need to be included.

C. Rear Contact Optimization

Various TCOs including ITO, AZO, and IZO (indium zinc oxide) have been applied as the transparent rear contact on perovskite solar cells using the sputtering method [4], [11], [12]. To prevent sputtering damage to the organic hole transport layer, a common method is to apply a thin layer of MoO_x prior to the TCO deposition. MoO_x is chosen because of its favorable band energy alignment for hole extraction. This method has been widely used in organic solar cells and, recently, in silicon solar cells [25]–[28].

The thickness of the MoO_x interlayer needs to be optimized. MoO_x that is too thick cannot fully cover the surface of the organic hole transport layer resulting in damage during MoO_x, and the electrode will reduce the oxidation states of the layer within the first few nanometers and make the film less conductive [29]. MoO_x that is too thick will increase the series resistance and parasitic optical absorption and greatly influence the overall tandem efficiency. The work function and conductivity MoO_x layer change under air exposure within an hour [30], [31]. In this work, it is found that a long waiting time between MoO_x deposition and ITO deposition has a detrimental effect on the semitransparent cell performance, which normally shows up as

the S-shape in the I–V characteristic of the device (see Fig. S5 in the supplementary material). Sputtering of ITO within an hour of MoO_x deposition is required to achieve the good semitransparent perovskite cell performance.

Sputtering conditions including RF power, chamber pressure, and duration need to be carefully chosen to limit the damage from the ion bombardment and UV exposure from the sputtering process, while at the same time achieving the desired conductivity and transparency. Again, the chamber pressure is fixed at 1.5 mtorr, while RF power and duration are varied. Due to the limited thermal budget of the organic layers in a perovskite cell, the rear TCO cannot be annealed at high temperature to improve the optical and electrical property as was done for the front TCO. Instead, we add a metal grid to compensate for the high sheet resistance of the rear contact. The addition of the grid increases the optical loss by a few percent due to shading. The metal grid is deposited by electron-beam evaporation through a shadow mask to avoid the use of photoresists or solvents that could degrade the device layers.

The finest metal width we can achieve with this method is 30–35 μm, which lies within the range of interest. The pitch is chosen as 1 mm, which is close to the optimal value to achieve the balance between resistive loss from TCO, metal grid, and the optical loss from shading (see Fig. S6 in the supplementary material).

Sputtered ITO with varying sheet resistance and solar weighted transmittance are plotted in Fig. 1(b) to evaluate the
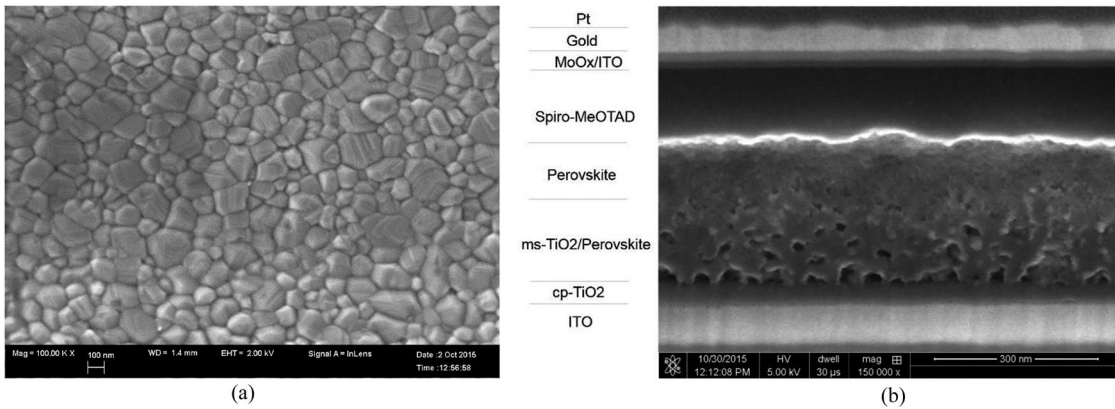
Fig. 3. (a) SEM surface image of perovskite film on ms-TiO$_2$ layer. (b) SEM cross-sectional image of semitransparent cell with no MgF$_2$. Note that the Gold and Pt layers at the top of the figure were deposited to protect the cell during FIB milling and are not present in the working cell.

potential tandem efficiency. The line connecting the dots represents the effect of adding a metal grid with ∼3% shading loss onto the layer. From the power loss analysis, high sheet resistance of the transparent contact up to 1000 $\Omega/\square$ can be compensated with the use of a metal grid to minimize the resistive loss in the top cell. In that range of sheet resistance, the transmittance of the layer needs to be prioritized to achieve higher tandem efficiency. Transmittance can be increased by lowering the RF power and/or shortening the duration of the deposition. However, the film will not be continuous with a very short deposition time, as illustrated in the case with 30 W of RF power and 900-s duration, where the high sheet resistance could not be compensated with the use of a metal grid. As the result, sputtered ITO at RF power of 30 W and 3600-s duration offer the best power fraction of close to 97%.

The power loss calculation does not take into account the damage to the perovskite cell due to sputtering under various conditions. Obvious damage is observed in the cross-sectional scanning electron microscopy (SEM) image of the perovskite cell with 60-W RF power and 3600-s duration. As the result, semitransparent perovskite cell with 60-W RF power has lower FF compared with the cell with 30-W RF power (see Fig. S7 in the supplementary material).

D. Semitransparent Perovskite Cell Performance

Fig. 3(a) shows a SEM image of the surface of the perovskite film grown on top of the mesoporous TiO$_2$ layer on the sputtered ITO glass substrate. Fig. 3(b) shows a SEM cross-sectional image of the semitransparent cell with all the layers as labeled. In the complete device, MgF$_2$ is deposited at both the front and rear sides to reduce the reflection loss. The perovskite layer is deposited using a solvent engineering method, which has been demonstrated previously with high-efficiency perovskite cells, producing uniform pinhole-free films [32], [33]. The continuous perovskite capping layer on top of the mesoporous TiO$_2$ enables the deposition of a uniform planar Spiro-MeOTAD hole transport layer, which prevents possible shunting paths. With the very thin protective MoO$_x$ layer, no obvious damage to the Spiro-MeOTAD is observed.

In good agreement with the power loss analysis and optimization process, the best results are obtained with RF power 90 W/duration 3600 s for the front contact and RF power 30 W/duration 3600 s for the rear contact with 10 nm of MoO$_x$ interlayer. Fig. 4(a) presents the performance of the semitransparent perovskite cell. The J–V measurement using a reverse scan at 50 mV/s gives good agreement with the steady-state measurement at the maximum power point. The steady-state current and time-dependent power output are presented in Fig. S8 in the supplementary material. The semitransparent cell has lower V_{oc} and J_{sc} compared with an opaque cell of the same structure, but with the MoO$_x$/ITO rear contact replaced by a gold electrode, as shown in Fig. 4(b). The reduction of J_{sc} is mainly due to the nonabsorbed light in the first pass not being reflected back to the perovskite active layer for photocurrent generation in the semitransparent device. However, this is not a significant concern as this light is instead transmitted to the bottom Si cell. The lower V_{OC} of the semitransparent cell might be attributed to the change in the interface from HTL/Au to HTL/MoO$_x$/ITO. Although several groups have reported an improvement of V_{oc} in semitransparent devices, no explanation has been given [9], [11]. The FF of the semitransparent cell is comparable with the opaque cell, which indicates that the lateral conductivity of the transparent contact and metal grid at the rear side does not increase the series resistance too much and that the organic HTL layer is not damaged by sputtering. In Fig. 4(b), the hysteresis effect on semitransparent cell is observed to be much less severe than the opaque cell. We believe this might come from the difference of the HTL interfaces, although further investigation needs to be undertaken. In the J–V scan of the opaque cell in the reverse direction, a reduction of the current density when the applied voltage changes from 0.2 to 0 V is observed. This might be related to the anomalous hysteresis effect of perovskite solar cells, but a detailed explanation does not exist at the moment.

Fig. 5(a) shows the optical characteristics of the complete cell, which exhibits broadband transmittance exceeding 80% in the 800–1000-nm wavelength range. Despite the use of MgF$_2$ antireflection coatings on both sides, the reflectance is still higher than 10% at some wavelengths due to the refractive index
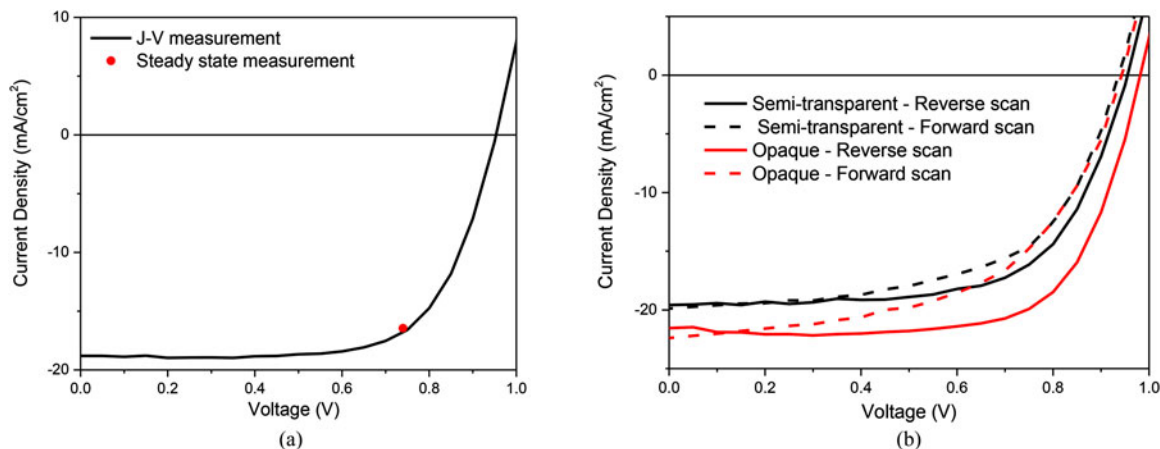
Fig. 4.   (a) *I–V* characteristic of semitransparent perovskite cell obtained by reverse scan with the rate of 50 mV/s. The dot presents the steady-state measurement at the maximum power point. (b) Comparison of hysteresis in the semitransparent cell and an opaque cell fabricated using the same process.
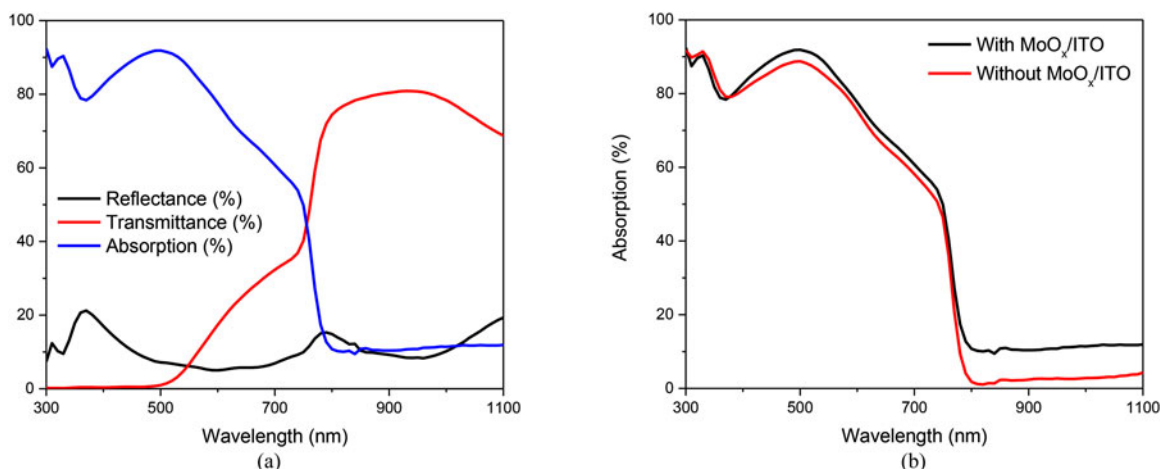
Fig. 5.   (a) Transmittance/reflectance/absorption data of the semitransparent perovskite cell. (b) Absorption of the device increase significantly with the addition of MoOx/ITO at the rear contact. The complete structure of the sample is Glass/ITO/cp-TiO2/ms-TiO2/Perovskite/Spiro/MoOx/ITO.

mismatch of multiple layers in the device. The complete semi-transparent cell absorbs up to 12% of incident light between 800–1100 nm, which is much lower than the absorption of 30–40% reported in other works [8], [12]. The absorption mainly comes from the MoO_x/ITO layers at the rear side [see Fig. 5(b)]. This increases the absorption by 7–8%, which is much higher than the absorption of the as-deposited ITO layer (<3%). With the negligible absorption from the 10-nm MoO_x, it implies that the electric field distribution inside the device is modified upon the adding of those layers, which increases the absorption of the device substantially.

E. Tandem Cell Performance

The silicon cell used in this work has a passivated emitter rear locally diffused (PERL) structure with an efficiency of 19.6%. The active area of the semitransparent perovskite cell is 5 mm × 5 mm, while the size of the PERL cell is 2 cm × 2 cm. Due to the cell size mismatch, the *J–V* characteristics of perovskite cell and silicon cell cannot be measured simultaneously. To

determine the value of J_{SC} for the silicon cell, several groups have proposed a two-step method, where the external quantum efficiency (EQE) of the Si cell (with the light incident on the Si cell filtered by the Perovskite cell) is measured first, followed by the determination of J_{sc} on the basis of the EQE spectrum. The *J–V* characteristic of silicon cell is then measured with an adjusted light intensity so that the measured J_{SC} matches the value determined from the EQE spectrum [8], [9]. This method will result in some inaccuracy as it does not account for the change in the solar spectrum when only infrared light can be transmitted through the perovskite filter. In this study, a 2.5 cm × 2.5 cm perovskite optical filter with the same layers and prepared under the same processing conditions as the semitransparent perovskite solar cell is used as the mask to directly measure the silicon cell performance under 1-sun illumination. The results are presented in Fig. 6. Under the perovskite cell filter, the current of the PERL cell obtained from the *J–V* measurement is 16.9 mA/cm^2, which agrees well with the current value calculated from the EQE data of 17.4 mA/cm^2. It is noticeable that the EQE value of filtered

	J_{sc} (mA/cm^2)	V_{oc} (V)	FF	Efficiency (%)
Semi-transparent perovskite cell	18.8	0.95	0.69	12.4
Semi-transparent perovskite cell - steady state				12.2
PERL silicon cell	39.1	0.66	0.76	19.6
PERL silicon cell - filtered	16.9	0.64	0.73	7.9
Tandem cell				20.1

(c)
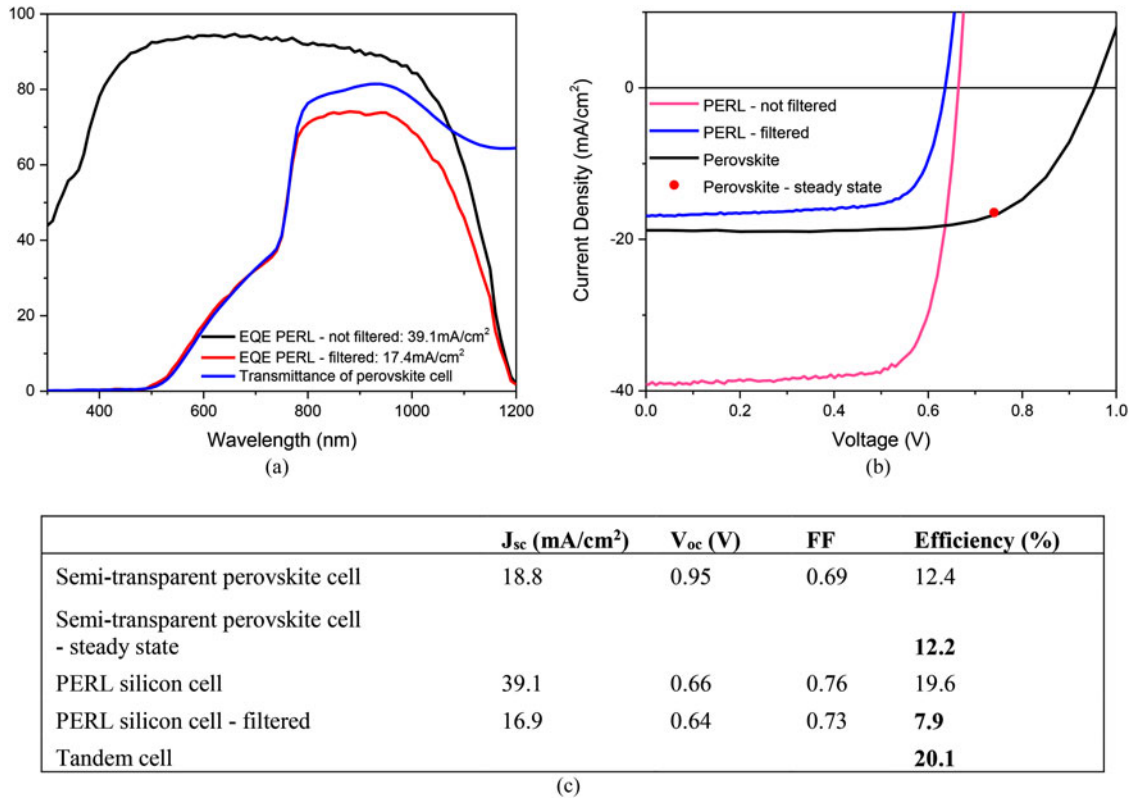
Fig. 6. (a) EQE of PERL silicon cell with and without filter and transmittance of perovskite cell. (b) *I–V* curves of PERL silicon cell with and without filter and semitransparent perovskite cell. (c) Summary of semitransparent perovskite cell, filtered, and nonfiltered PERL cell and tandem cell performance.

silicon is higher than the transmittance of the semitransparent perovskite at some wavelength range. This can be explained as the transmittance measurement of the perovskite cell takes into account the shading effect of applied metal grids, which causes around 3% reduction in the transmittance. The shading effect is excluded during the EQE measurement as the small beam size is aligned in between two metal fingers. The V_{oc} of the PERL cell is reduced by 20 mV as a result of the lower light intensity. The reduction of the Si cell FF by 3% can be explained by the greater impact of the cell shunt resistance at the lower current density. Overall, the efficiency of the PERL cell under the perovskite filter is 7.9%. The four-terminal tandem efficiency is calculated as the sum of perovskite top cell and filtered PERL silicon bottom cell with a value of 20.1%. The result is promising as the tandem gives a net improvement of 0.5% compared with the stand-alone PERL cell. To date, this is one of the highest efficiencies reported for perovskite on silicon tandem to our knowledge.

F. Challenges and Outlook

According to previous work, with a bandgap of 1.55 eV for the active material, a perovskite top cell efficiency of 17% is required to achieve 25% perovskite-on-silicon tandem efficiency. The silicon cell after being filtered by perovskite cell needs to contribute the remaining 8%. By replacing the 19.6% PERL cell with a more efficient interdigitated back contact cell with initial efficiency of 23.3%, we can achieve an efficiency of 9.2% with a perovskite filter (see Fig. S9 in the supplementary

material). Thus, the main challenges are increasing the efficiency and further increasing the transparency of the semitransparent perovskite cell. The reduction of V_{OC} in our current cells might be minimized by interface engineering the layers at the rear contact, while the J_{SC} might be improved with a thicker perovskite layer. Optical modeling of the semitransparent perovskite cell was performed, which provides a good fit to experimental data (see Fig. S10 in the supplementary material). A schematic of the semitransparent perovskite cell is shown in the inset of Fig. 7, where layer thicknesses shown were obtained by fitting the model to the measured reflection/transmission of the complete cell. The optical model was used to calculate the optical absorption in each layer of the cell, shown in Fig. 7, where the current loss was obtained by integrating the absorption, weighted by the AM1.5G photon flux. The three primary current loss mechanisms are reflection from the perovskite cell, absorption within the rear MoO_x/ITO contact layers, and absorption within the Spiro layer where each mechanism reduces the potential current by 2.33, 1.39, and 0.85 mA/cm^2, respectively. The reflectance needs to be reduced by using better antireflectance coating method and reducing the refractive index mismatch inside the device, especially for longer wavelengths. A method for optically coupling the perovskite and silicon cell also needs to be implemented to avoid light escaping before reaching the bottom cell. Optimization of MoO_x thickness for the rear contact is expected to further improve the transparency. Reducing the hole-transport layer thickness as much as possible without degrading the perovskite cell performance will help to
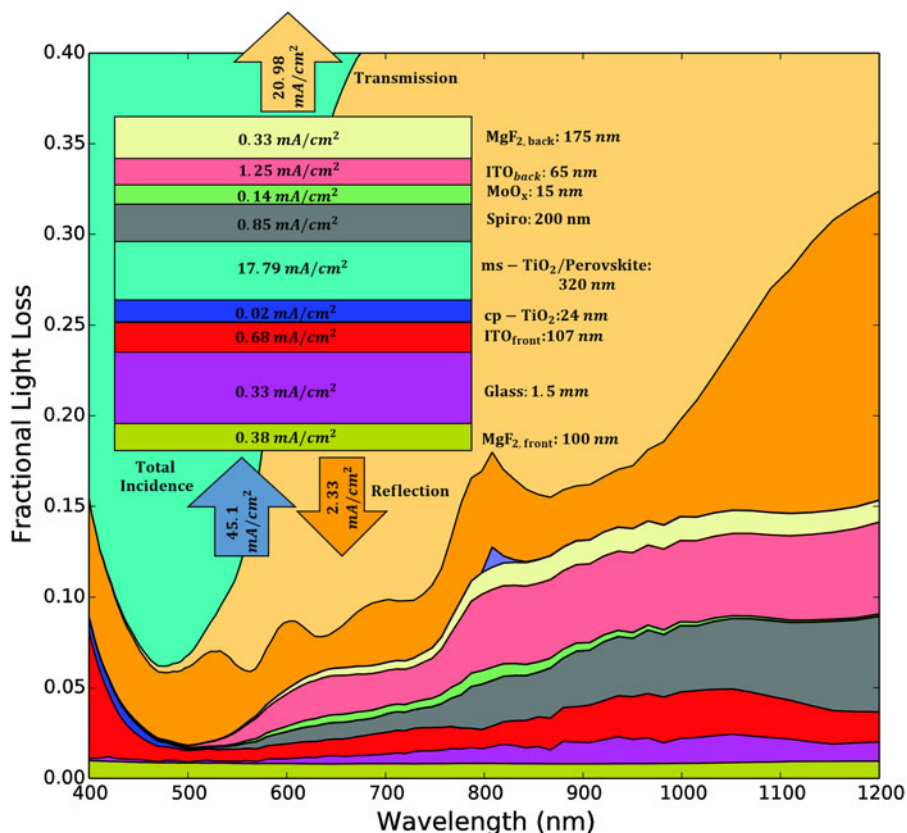
Fig. 7. Fractional light loss breakdown of all the layers in the semitransparent perovskite cell together with reflectance and transmission (the *y*-axis is truncated for clarity; refer to Fig. S11 in the supplementary material for the full picture). (Inset) Schematic of the device. All the layer thicknesses were estimated from the optical model, and the calculated current loss from each layer is shown on each layer, together with the total incidence, reflected, and transmitted current as the arrows.

reduce the current loss from this layer [34]. Another strategy is to increase the bandgap of the perovskite active material, as this will lessen the requirement for the top cell efficiency since more light will be transmitted to the bottom cell.

Increasing the size of the perovskite cell to match the size of silicon cell without affecting the cell performance is challenging especially when spin-coating is used as the deposition method. New perovskite deposition methods such as slot die coating or antisolvent extraction are required to fabricate efficient large-area perovskite cells [35]. One of the biggest challenges is to improve the stability of perovskite cells to be comparable with that of silicon.

III. CONCLUSION

In conclusion, a semitransparent perovskite cell with 12.2% steady-state efficiency and broadband transmittance over 80% has been demonstrated through the optimization of sputtered ITO for front and rear transparent contacts. This enables perovskite-on-silicon tandem efficiency of 20.1% using a 19.6% PERL silicon cell. This work provides clear guidelines and practical methods to optimize transparent contact for perovskite solar cells. Future work is expected to lead to >25.6% tandem efficiency.

REFERENCES

[1] [Online]. Available: http://www.nrel.gov/ncpv/images/efficiency_chart.jpg
[2] J. H. Noh, S. H. Im, J. H. Heo, T. N. Mandal, and S. I. Seok, "Chemical management for colorful, efficient, and stable inorganic–organic hybrid nanostructured solar cells," *Nano Lett.*, vol. 13, pp. 1764–1769, 2013.
[3] N. N. Lal, T. P. White, and K. R. Catchpole, "Optics and light trapping for tandem solar cells on silicon," *IEEE J. Photovoltaics*, vol. 4, no. 6, pp. 1380–1386, Nov. 2014.
[4] M. Filipič *et al.*, "CH 3 NH 3 PbI 3 perovskite/silicon tandem solar cells: characterization based optical simulations," *Opt. Exp.*, vol. 23, pp. A263–A278, 2015.

[5] P. Loper *et al.*, "Organic–inorganic halide perovskites: Perspectives for silicon-based tandem solar cells," *IEEE J. Photovoltaics*, vol. 4, no. 6, pp. 1545–1551, Nov. 2014.

[6] J. P. Mailoa *et al.*, "A 2-terminal perovskite/silicon multijunction solar cell enabled by a silicon tunnel junction," *Appl. Phys. Lett.*, vol. 106, art. no. 121105, 2015.

[7] S. Albrecht *et al.*, "Monolithic perovskite/silicon-heterojunction tandem solar cells processed at low temperature," *Energy Environ. Sci.*, vol. 9, pp. 81–88, 2016.

[8] P. Löper *et al.*, "Organic–inorganic halide perovskite/crystalline silicon four-terminal tandem solar cells," *Phys. Chem. Chem. Phys.*, vol. 17, pp. 1619–1629, 2015.

[9] C. D. Bailie *et al.*, "Semi-transparent perovskite solar cells for tandems with silicon and CIGS," *Energy Environ. Sci.*, vol. 8, pp. 956–963, 2015.

[10] Z. Hawash, L. K. Ono, S. R. Raga, M. V. Lee, and Y. Qi, "Air-exposure induced dopant redistribution and energy level shifts in spin-coated spiro-MeOTAD films," *Chem. Mater.*, vol. 27, pp. 562–569, 2015.

[11] L. Kranz *et al.*, "High-efficiency polycrystalline thin film tandem solar cells," *J. Phys. Chem. Lett.*, vol. 6, pp. 2676–2681, 2015.

[12] J. Werner *et al.*, "Sputtered rear electrode with broadband transparency for perovskite solar cells," *Sol. Energy Mater. Sol. Cells*, vol. 141, pp. 407–413, 2015.

[13] E. Della Gaspera *et al.*, "Ultra-thin high efficiency semitransparent perovskite solar cells," *Nano Energy*, vol. 13, pp. 249–257, 2015.

[14] D. Bryant *et al.*, "A transparent conductive adhesive laminate electrode for high-efficiency organic-inorganic lead halide perovskite solar cells," *Adv. Mater.*, vol. 26, pp. 7499–7504, 2014.

[15] P. You, Z. Liu, Q. Tai, S. Liu, and F. Yan, "Efficient semitransparent perovskite solar cells with graphene electrodes," *Adv. Mater.*, vol. 24, pp. 3632–3638, 2015.

[16] Y. Yang *et al.*, "Multilayer transparent top electrode for solution processed perovskite/Cu (In, Ga)(Se, S) 2 four terminal tandem solar cells," *ACS Nano*, vol. 9, pp. 7714–7721, 2015.

[17] T. P. White, N. N. Lal, and K. R. Catchpole, "Tandem solar cells based on high-efficiency c-Si bottom cells: Top cell requirements for > 30% efficiency," *IEEE J. Photovoltaics*, vol. 4, no. 1, pp. 208–214, Jan. 2014.

[18] J. Zhao, A. Wang, M. A. Green, and F. Ferrazza, "19.8% efficient "honeycomb" textured multicrystalline and 24.4% monocrystalline silicon solar cells," *Appl. Phys. Lett.*, vol. 73, pp. 1991–1993, 1998.

[19] Y. Hu, X. Diao, C. Wang, W. Hao, and T. Wang, "Effects of heat treatment on properties of ITO films prepared by rf magnetron sputtering," *Vacuum*, vol. 75, pp. 183–188, 2004.

[20] L. Cruz, C. Legnani, I. Matoso, C. Ferreira, and H. Moutinho, "Influence of pressure and annealing on the microstructural and electro-optical properties of RF magnetron sputtered ITO thin films," *Mater. Res. Bull.*, vol. 39, pp. 993–1003, 2004.

[21] V. Zardetto, T. M. Brown, A. Reale, and A. Di Carlo, "Substrates for flexible electronics: A practical investigation on the electrical, film flexibility, optical, temperature, and solvent resistance properties," *J. Polymer Sci. B, Polymer Phys.*, vol. 49, pp. 638–648, 2011.

[22] M. Alam and D. Cameron, "Investigation of annealing effects on sol–gel deposited indium tin oxide thin films in different atmospheres," *Thin Solid Films*, vol. 420, pp. 76–82, 2002.

[23] M. Alam and D. Cameron, "Optical and electrical properties of transparent conductive ITO thin films deposited by sol–gel process," *Thin Solid Films*, vol. 377, pp. 455–459, 2000.

[24] J. George and C. Menon, "Electrical and optical properties of electron beam evaporated ITO thin films," *Surface Coatings Technol.*, vol. 132, pp. 45–48, 2000.

[25] H. Schmidt *et al.*, "Efficient semitransparent inverted organic solar cells with indium tin oxide top electrode," *Appl. Phys. Lett.*, vol. 94, art. no. 243302, 2009.

[26] V. Shrotriya, G. Li, Y. Yao, C.-W. Chu, and Y. Yang, "Transition metal oxides as the buffer layer for polymer photovoltaic cells," *Appl. Phys. Lett.*, vol. 88, art. no. 073508, 2006.

[27] S. M. Park, Y. H. Kim, Y. Yi, H.-Y. Oh, and J. W. Kim, "Insertion of an organic interlayer for hole current enhancement in inverted organic light emitting devices," *Appl. Phys. Lett.*, vol. 97, art. no. 063308, 2010.

[28] C. Battaglia *et al.*, "Silicon heterojunction solar cell with passivated hole selective MoOx contact," *Appl. Phys. Lett.*, vol. 104, art. no. 113902, 2014.

[29] M. T. Greiner and Z.-H. Lu, "Thin-film metal oxides in organic semiconductor devices: their electronic structures, work functions and interfaces," *NPG Asia Mater.*, vol. 5, art. no. e55, 2013.

[30] I. Irfan, A. J. Turinske, Z. Bao, and Y. Gao, "Work function recovery of air exposed molybdenum oxide thin films," *Appl. Phys. Lett.*, vol. 101, art. no. 093305, 2012.

[31] I. Irfan and Y. Gao, "Effects of exposure and air annealing on MoOx thin films," *J. Photon. Energy*, vol. 2, pp. 021213-1–021213-12, 2012.

[32] N. J. Jeon *et al.*, "Solvent engineering for high-performance inorganic–organic hybrid perovskite solar cells," *Nature Mater.*, vol. 13, pp. 897–903, 2014.

[33] N. J. Jeon *et al.*, "Compositional engineering of perovskite materials for high-performance solar cells," *Nature*, vol. 517, pp. 476–480, 2015.

[34] N. Marinova *et al.*, "Light harvesting and charge recombination in $CH_3NH_3PbI_3$ perovskite solar cells studied by hole transport layer thickness variation," *ACS Nano*, vol. 9, pp. 4200–4209, 2015.

[35] M. Yang *et al.*, "Square-centimeter solution-processed planar CH3NH3PbI3 perovskite solar cells with efficiency exceeding 15%," *Adv. Mater.*, vol. 27, pp. 6363–6370, 2015.

Authors' photographs and biographies not available at the time of publication.